行政院原子能委員會

委託研究計畫研究報告

【太陽能及乙醇／氫氣轉換之量子化學計算模擬及實驗驗證】

【Quantum Simulations of Solar Energy and Ethanol to Hydrogen Conversion Processes with Experimental Validations】

目　錄

I

中文摘要

本計畫是為期三年行政院原子能委員會委託研究計畫之第二年執行結果摘要。這一年主要的工作在進行以下兩個目標：1. 利用大型電腦計算解釋 InN/TiO_2 太陽能電池的製作機制及 InN 與 TiO_2 之間利用量子點及有效的化學鍵製作方法。2. 理論與實驗驗證 L. D. Schmidt 的 Rh/CeO_2 乙醇轉換氫氣催化劑的性能，並進而研究發現新而便宜的催化劑。

在乙醇轉換氫的實驗上，Schmidt 的 Rh/CeO_2 實驗結果已完全證實用乙醇與水的混合物目前已得到 115%的轉換率，實驗比較粉狀、方型與棍狀的 CeO_2 奈米結晶效率的差異已完成，且研究 CeO_2 與 ZrO_2 混合氧化物的實驗已在進行中。

大型量子計算可分為三方面，1. 乙醇轉氫在不同催化劑表面反應基制的研究。2. 量子點在 TiO_2 表面吸附的能量與結構。3. 發展 SCC-DFTB 應用於乙醇轉氫及量子點/TiO_2 方面的大型計算。

在乙醇轉氫方面的計算，今年主要在了解水氣轉氫 $(CO+H_2O \rightarrow CO_2 +H_2)$在 Rh/CeO_2 上的反應機制及能量。也進行乙醇在 $Rh/CeO_2/ZrO_2$ 催化劑上的吸附及分解，同時，CuO/Al_2O_3 對乙醇轉氫的可行性也在計算中。

在量子點/TiO_2 系統的計算，今年著重於$(InN)_x/TiO_2$ 及$(Si)_x/TiO_2$ 兩系統的研究，量子點的大小影響 TiO_2 帶隙的計算，已供給良好的結果。

在 SCC-DFTB 程式的發展，目前也有很好的進展，這個程式的完成，將可供給本計算團隊用 VASP 及 CASTEP 以外作大型分子

群的計算。

除了上述的計算外，$In(CH_3)_3$ 與 HN_3、NH_3、H_2O_2 及 H_2S 的氣相反應機制及能量變化已計算完畢，此系列的反應，與 InN、InO_x 及 InS_x 的沉積有關。

Abstract

This is the report for the second of the 3-year research project on the computational and experimental studies of the InN/TiO$_2$ system and/or the catalytic conversion of ethanol to hydrogen by Schmidt's technique employing the Rh/CeO$_2$ catalyst. Our goals are two-fold: 1. Utilization of the large scale computation to elucidate processes relevant to the InN/TiO$_2$ solar cell system including quantum-dot and chemical functional-group modifications of the InN-TiO$_2$ interface; 2. Experimental and computational studies of Schmidt's ethanol to H$_2$ conversion processes in order to search for cheaper and equally efficient catalysts.

For the ethanol to H$_2$ conversion studies, Schmidt's Rh/CeO$_2$ catalytic conversion data have been fully duplicated with up to 115% conversion from autothermal oxidation with mixtures of C$_2$H$_5$OH and H$_2$O. Studies have been completed on different nanocrystal forms of CeO$_2$ (powder, cube and rod) on the efficiency of the H$_2$ conversion; conversions greater than 125% have been reached using the rod form of the catalyst.

Computationally, we have focused on three aspects: 1. Catalytic conversion of ethanol to H$_2$; 2. Electronic structures of quantum dots (QDs) attached to TiO$_2$ nanoparticles; 3. Development of the SCC-DFTB (self-consistent charge-density functional theory tight-binding) method for large cluster calculations.

For the ethanol to hydrogen conversion related calculations, we have studied the H$_2$O+CO water-gas shift reaction on the Rh/CeO$_2$ catalyst. The reaction was found to be obeying the

Langmuir-Hinshelwood mechanism through chemisorption of both H_2O and CO on Rh (for CO) and/or Ce (for H_2O) sites, followed by the dissociation of $H_2O(a)$ and oxidation of CO(a) by HO(a). In addition, calculations for adsorption and decomposition of ethanol on Rh/CeO_2-ZrO_2 and CuO/Al_2O_3 have been done.

For the QD/TiO_2 related calculations, focus has been made on $(InN)_n/TiO_2$ (n=1-3) and $(Si)_x/TiO_2$ (x=1-67). The effects of QD-sizes on the system's band gap have been clearly elucidated.

For the development of the SCC-DFTB method, a basic code for the establishment of elemental parameters has been completed, and the effort on the conversion of binding properties of key elements such as Ti, B, Cl, Si, ….among others is being made.

Aside from the aforementioned large practical systems, we have also carried out detailed potential energy surfaces for reactions of $In(CH_3)_3$ with HN_3, NH_3, HO_2 and H_2S in the gas phase. These reactions may take place in the OMCVD of the corresponding QDs.

壹、計畫緣起與目的

有鑑於地球能源問題已開始受到重視，尋求相關取代能源已是迫不及待，而目前以燃料電池及太陽能電池為首要研究目標。在燃料電池方便，由於考慮到環保上相關的問題，因此希望發展出一套良好的乙醇轉換為氫氣的系統。希望此套系統能得到最高的轉換效率，並且不對環境造成破壞影響。目前此方向之研究又以 Schmidt 所得到的將近百分之一百的轉換為最優[1]，而此相關研究中，最理想的狀況下，甚至可以得到百分之三百的轉換效率，所以本次計劃將以此理論為根本，希望發產出更進一步的結果。

乙醇是一種"綠色"(環保)燃料，它可以利用糖或大豆等農產品發酵而製造。台灣的亞熱帶地理位置適合發展以乙醇作為未來可能的永續能源，尤其是在燃料電池的應用方面。很不幸的，乙醇無法直接地被用於燃料電池，因為它和碳氫化合物具有相同的碳原子位置的問題。燃燒電池除產生電能外，其副產物僅為水及熱能，因此具有低污染的優點，是一種可產生環保能源的方法。Schmidt 等人[1]所採用的一個策略就是利用貴重金屬，如：Pt 或 Rh 吸附在金屬氧化物，如：CeO_2 或 La_2O_3 上面。他們利用在陶瓷泡狀結構上的 Rh/CeO_2 觸媒可以達到 95% 以上之轉化率。他們利用乙醇和水的混合物，藉由眾所周知的水煤氧反應 $CO + H_2O \rightarrow CO_2 + H_2$ 之助，可以達到 115%的轉化率。這些令人振奮的結果顯示利用乙醇這種真正環保且不多產生 CO_2 的燃料來取代日漸昂貴且對環境極具殺傷力的石化燃料，如石油和天然氣，已經變為可能。

在太陽能電池的研究方面，最近，主持人與其研究群藉由有

機金屬化學沉積的方式 TiO₂ 的奈米粒子上成長出不同厚度且品質優良的 InN 薄膜[2]，吸收光譜顯示吸收波段為 UV/visible 範圍內 390 nm 到 800 nm 波長的寬廣吸收。為了了解 InN 光敏化 TiO₂ 奈米粒子薄膜的結構與電子能態及對吸收波長的影響以及促進電子由 InN 移轉到 TiO₂ 奈米薄膜的效率，量子點及有效的化學鍵，諸如 Si 及 InP 量子點和-BOO、-POO、>SiOO 等化學根在 TiO₂ 表面吸附能量必須估計。這類資料必須利用新進的量子計算軟體與高速電腦的工率才能得知，故與國網中心的合作是非常必要的，因為台灣在這方面的大型計算尚遠落後於日本、美國及歐盟國家。

以超級電腦進行大尺度的計算以模擬相關化學反應及物理現象已經變成尖端材料研究及元件製造的一個不可或缺的部份。此種模擬計算可以幫助吾人瞭解所欲研究的系統中支配的物理法則及化學機制，因而提昇研究品質及產品開發的效率。在這方面，台灣是遠落於美國、日本和歐洲之後。為了增進台灣利用大型計算的能力，尤其是改進 InN/TiO₂ 奈米粒子太陽電池之製程及效率[1]以及乙醇-氫氣的催化轉化效率，我們擬模擬 InN 薄膜沉積的反應，尤其是將重點放在利用自組官能基形成奈米量子點的過程，並研究其與不同頻帶邊(band edge)之金屬氧化物混合之效應。我們也將研究乙醇催化轉化成氫氣的機制，希望能夠找到一個比最近 Schmidt 等人[2]所提出來的 Rh/CeO₂ 更為價廉且更具效率的非均相觸媒。

此計劃將專注於利用最先進的量子化學計算，系統化地研究在含有 Si, InP 及其他金屬氧化物量子點的 InN/QDs/TiO₂ 系統中，使 TiO₂ 奈米粒子表面官能化的反應機構以及乙醇在吸附在 CeO₂, La₂O₃, Al₂O₃ 等金屬氧化物基質的貴重金屬(如: Rh, Pt, Pd)的轉化機

制，並比較不同金屬的催化效率，以瞭解其催化的基本物理及化學原理。一旦催化劑的催化明確性以及其金屬氧化物基質的關連作用被瞭解，則我們可以利用量子化學理論計算探尋較具經濟效益的金屬催化物及其金屬氧化物基質；吸附在 Al_2O_3, TiO_2 或 MgO 等奈米粒子上面的 Zn, Fe, Co, Cu 或 Ag 金屬奈米粒子的催化作用將會被仔細地研究。為了落實理論計算的結果，我們亦將利用一個類似 Schmidt 等人[1]所使用的小型的反應系統，以實驗來測量理論計算所建議的觸媒及其金屬氧化物基質的乙醇轉化效率。理論與實驗相結合來研究 InN/TiO_2 沉積以及乙醇-氫氣轉化過程，將可對其將來在工業上的應用提供寶貴的資訊。

貳、研究方法與過程

一、乙醇轉氫機制的計算：

(一) J. J. Ho（何嘉仁）：

Theoretical Investigation of the Water-Gas Shift (WGS) Reaction over a $4Rh/CeO_2$ (111) Surface

1. $4Rh/CeO_2$ (111)-(2×2) clean surface

關於四個 Rh 原子單層吸附在 CeO_2(111)-(2×2)之厚層模型計算，其可能的結構呈現在 Figure 1。經密度泛函理論幾何優選計算後可能的原子吸附結構，包括：$4Rh/CeO_2$(Rh-Ce)、$4Rh/CeO_2$(Rh-O_u)、$4Rh/CeO_2$(Rh-O_d)和 $4Rh/CeO_2$(Rh-cluster) 四種情形，其平均每顆 Rh 原子吸附能大小依次為 63.88、68.95、71.26 和 91.78 kcal/mol，由此計算結果可知 $4Rh/CeO_2$(Rh-cluster)為最穩定的模擬表面。我們將選擇這個表面做為 water-gas-shift reaction 的基質。前述四種吸附結構的平均吸附能和 Bader charge [3]記錄於 Table 1 中。根據 Bader's method 的電子密度計算發現，當 Rh 金屬吸附在表面氧原子上方時(O_u,O_d 或 4Rh-cluster)，其電性都比較趨近於中性-約 +0.16~0.38|e|，然而當吸附在 Ce 原子上方時 ($4Rh/CeO_2$(Rh-Ce))，其所帶電荷較偏向於正電-平均為 +0.60|e|。對於何以會造成如此的差別，我們提出一些想法:當 Rh 原子吸附在表面 O 原子上方時，因 O 原子電負度大於金屬的 Rh 原子，所以會將電子由 Rh 端拉往 O 端，而此時 O 原子的電荷密度已高，故會將其孤對電子反向提供(back donation) 到空的 Rh 原子 d 軌域，因而產生 Rh 原子較偏中性的結果;然

而在原先已帶+4 價的 Ce 原子上方,則較容易拉 Rh 原子的電子雲,而沒有電子反向提供(back donation)的現象,造成其 Rh 原子偏向帶正電的結果。
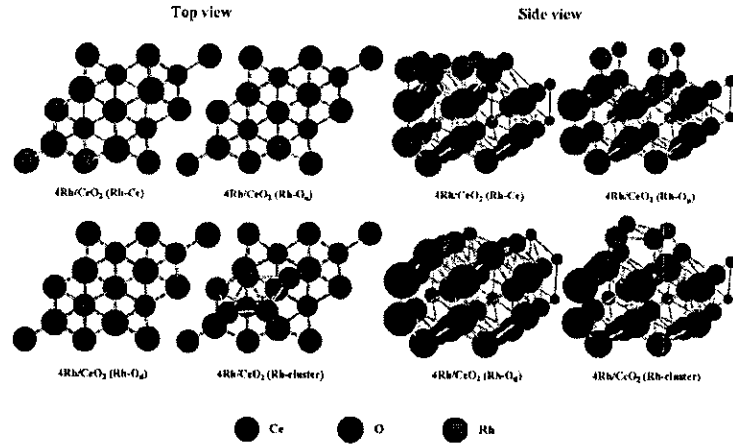

Figure 1. Top and side views of a monolayer of Rh coverage on a slab model of a $CeO_2(111)-(2\times2)$ surface. The blue, red and green spheres represent Ce, O and Rh atoms, respectively. $Rh-O_d$ represents that the Rh atoms are directly on top of oxygen atoms located at the down-side positions, whereas $Rh-O_u$ are at the upper-side positions.

T	$4Rh/CeO_2$ (Rh–Ce)	$4Rh/CeO_2$ (Rh–O_u)	$4Rh/CeO_2$ (Rh–O_d)	$4Rh/CeO_2$ (Rh–cluster)
a E_{ads} / kcal mol^{-1}	63.88	68.95	71.26	91.78
b Charge of Rh /e	0.60	0.16	0.38	0.20
l a. $Eads = - [E(4Rh/CeO_2) - 4*E(Rh) - E(CeO_2)] / 4$				

Table 1. Mean adsorption energies[a] and Bader charges of monolayer Rh adsorbed on a $CeO_2(111)$ surface

2. Adsorption geometries and energetics

我們探討 CO 和 H_2O 吸附於 $4Rh/CeO_2$(Rh-cluster)表面的穩定結構,幾何優選計算後的結果描繪於 Figure 2 中;檢視 $4Rh/CeO_2$(Rh-cluster)表面,我們可以把表面的 Rh 原子視其所

在環境的對稱性分為兩種，分別標示為 Rh_a 和 Rh_b。各個吸附位置其鍵長、鍵角和吸附能表列於 Table 2 中。觀察五種列於 Table 2 的可能吸附結構和吸附能可知，一氧化碳能與表面 Rh 金屬形成強烈的鍵結，且鍵結形式為利用碳端和 Rh_a 原子相接。而一氧化碳與過渡金屬元素的鍵結機制則可以用 Blyholder model [4] 來說明：當一氧化碳以碳端與過渡金屬元素鍵結時，一氧化碳利用 5σ 軌域提供電子給予表面 Rh 原子，表面的 Rh 原子則利用其 d 軌域電子反向提供(back donation)電子到一氧化碳分子的 $2\pi^*$ 軌域，因此可形成穩定的 $OC\text{-}Rh_{a(a)}$ 鍵結。另一方面，經由計算的結果發現，水分子較易利用其上的 O 原子和表面的金屬原子(Rh 或 Ce 原子)相接，而不易與表面的 O 原子作用。當和表面的金屬原子作用時，水分子的吸附能大小為 13.1~24.2 kcal/mol，遠大於和表面 O 原子作用時的吸附能(與 O 原子作用時吸附能小於 1 kcal/mol)。這樣的結果是符合預期的，因為當(O...O)的結構形成時，會由於孤對電子間的斥力造成吸附結構的不穩定。
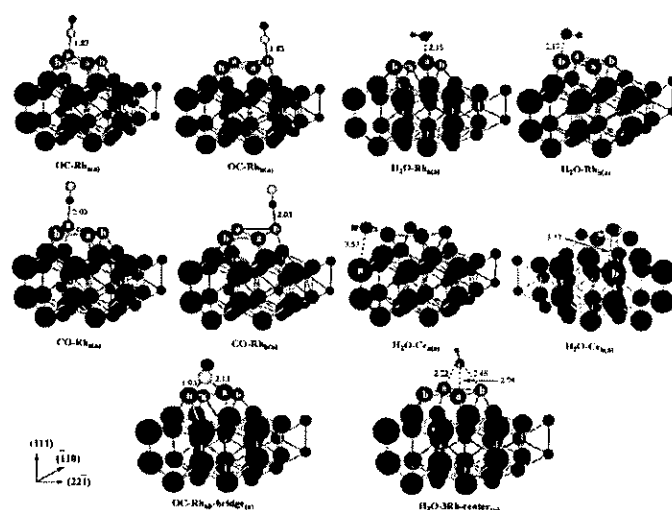

Figure 2. Calculated optimized conformations of CO and H_2O on the 4Rh/CeO₂ (Rh–cluster) surface. The bond lengths are given in Å.

Table 2. Optimized bond lengths and adsorption energies [a], E_{ads} (kcal/mol), for H_2O and CO on $4Rh/CeO_2$(Rh-cluster) surface, calculated for the slab model with VASP. Optimized structures are shown in Figure 2.

species	$r(Rh(Ce)-C(O))$ /Å	$r(O-C(H))$ /Å	$\angle(Rh-C(O)-O(C))$ /deg	E_{ads} /kcal mol^{-1}
$OC-Rh_{a(a)}$	1.83	1.17	177.0	67.44
$OC-Rh_{b(a)}$	1.83	1.17	174.8	61.07
$CO-Rh_{a(a)}$	2.03	1.16	177.5	13.88
$CO-Rh_{b(a)}$	2.03	1.16	175.5	6.98
$OC-Rh_{ab}-bridge_{(a)}$	1.93 (2.13)[b]	1.18	149.3 (130.6)[b]	62.66
$H_2O-Rh_{a(a)}$	2.15	0.98		24.20
$H_2O-Rh_{b(a)}$	2.17	0.99		16.72
$H_2O-Ce_{a(a)}$	3.53	0.99		17.54
$H_2O-Ce_{b(a)}$	3.57	1.00		13.57
$H_2O-3Rh-center_{(a)}$	2.22 (2.48, 2.94)[b]	0.98 (1.00)[b]		13.08

[a] $E_{ads} = - (E_{total} - E_{molecule} - E_{surface})$

[b] differential bond length and bond angle in another site

3. Potential–energy surfaces

關於 $4Rh/CeO_2$(Rh-cluster)表面對於 water-gas-shift reaction 催化效用的探討，我們提出了一條可行的反應機制，其所相對 potential-energy surface 描繪於 Figure 3 中。首先，由水分子斷一個 O-H 鍵開始，經由表面系統的催化，此步驟反應活化能的大小為 17.43 kcal/mol，而反應放熱 2.12 kcal/mol，生成 OH 和 H 中間產物吸附於表面。接著，OH 能夠和 CO 分子快速的反應產生 $HOOC-Rh_{a(a)}$，反應活化能僅僅只有 4.28 kcal/mol，且放熱 14.18 kcal/mol。我們比較 TS2 和中間產物的結構可以發現，在 TS2 結構中 C...O 的距離(2.65 Å)和中間產物間 C...O 的距離相近(2.79 Å)。根據 Hammond postulate [5]，經由 TS2 的

反應路徑為一"early"的過渡狀態，因此為一放熱反應且有較低的反應活化能。我們進一步比較 Liu 等作者[6]對於水氣轉移反應在 4Au/CeO$_2$(111)表面的研究，發現其在 CO 和 OH 結合的活化能也非常的低，只有約 2.4 kcal/mol，和我們的計算結果相當。第三步，由形成的 COOH 分子脫去 H 原子而釋放出 CO$_2$，此步驟反應活化能為 25.87 kcal/mol，吸熱 20.26 kcal/mol。最後一個步驟(H$_{(a)}$＋H$_{(a)}$ →H$_{2(g)}$)反應可由 large entropy 來做驅動，將可藉由提高溫度來克服。而我們所提出的水氣轉移反應經表面催化的機制，也被 Gorte 等作者[7]提及和討論過。
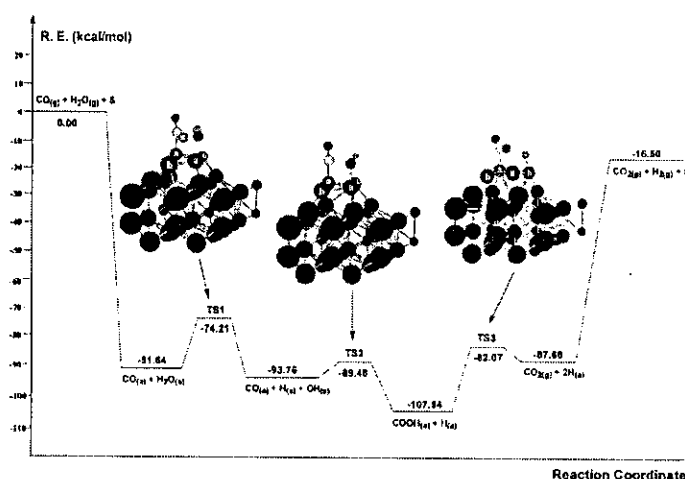
Figure 3. Calculated potential-energies for the reaction CO$_{(g)}$ + H$_2$O$_{(g)}$ → CO$_{2(g)}$ + H$_{2(g)}$ on a surface of 4Rh/CeO$_2$ (Rh–cluster)

(二) M. Hayashi（林倫年）：

我們提出了以 PBC-DFT 方法來針對 Al$_2$O$_3$ 表面幾何結構與能量的計算。同樣的方法也使用在 CO 與 H$_2$O 的吸附能上的計算，並將結果與先前的 VASP 計算作一比較。我們發現到，CO 吸附能與幾何結構的計算結果與 VASP 所得的十分接

近，然而 H_2O 的計算結果則不同。這表示在考慮 H_2O 分子的反應機構計算時，應該更加謹慎的選擇使用的計算模型。在 $Ce_{0.5}Zr_{0.5}O_2$ (111)表面的研究裡，使用 VASP 來計算結構最佳化。由於陽離子半徑的差異，造成了表面晶格的扭曲，而產生了反應的活性吸附位置。

1.目的

以 Gaussian 03 軟體為基礎的週期邊界條件-密度泛函數理論(PBC-DFT)，我們以此方法建立 Al_2O_3 表面與 CO 及 H_2O 之間吸附能量與幾何結構的計算。另一個目標是使用 VASP 建立 $Ce_{0.5}Zr_{0.5}O_2$ (111)表面，透過此計算希望能闡述化學反應的可能活性位置。

2.背景

鈰是目前已知能夠增強過渡金屬催化效果的金屬之一，特別是在水煤氣轉換(WGS)，水蒸氣重組氧化，以及 PROX(CO 的優氧化)等反應。最近，Schmidt 研究團隊發現乙醇轉化 H_2 的反應中，以 Rh-Ce 過渡金屬氧化物作為催化劑能提供更穩定與更大的水煤氣轉換活性。目前 Zr 與 CeO_2 或是 Al_2O_3 的摻雜系統也是重要的研究項目之一，因為這樣的系統具有較少的成本或是較高的強度。

3.方法

今年上半年，我們利用 Gaussian 03 量子化學軟體來檢驗以其週期邊界條件方法計算 γ-Al_2O_3 晶體與其(110C)表面的能

力。在此研究中，交換相干泛函數指定為 PW91PW91 並使用 STO-3G 與 3-21G 為基底函數以及密度適調近似法(DFA)。幾何結構最佳化以 PW91PW91/3-21G 等級計算，而能量則使用 6-31G*基底以得到更高的精確度。同時我們建立了(110C)表面的 slab 模型，此模型包含了 6 層原子以及 14Å 的真空層；其中上 3 層為可自由鬆弛，下 3 層則以其晶格參數固定。與經由鬆弛所有原子層的完全幾何結構最佳化差異僅在 1%以內。因此所有的計算將以此 slab 模型實行。CO 於不同位置的吸附能、以及不同數量的 H_2O 吸附能的計算，最後都將與 VASP 的結果比較[8-9]。

在下半年度，我們開始著手於 $Ce_{1-x}Zr_xO_2$ (111)與其摻入 Rh 原子的表面與乙醇反應的研究。我們希望能了解有 Rh 原子存在時，乙醇如何與 $Ce_{0.5}Zr_{0.5}O_2$ (111)表面反應。此研究使用 VASP 軟體，以 PW91 方法、cutoff=350eV 與 k-points=3x2x1 的條件下計算。首先得到 $Ce_{0.5}Zr_{0.5}O_2$ 的三維穩定結構，接下來以此最佳化晶體結構來建立(111)表面。

4.進展與結論

首先先針對 CO 與 $\gamma-Al_2O_3$(110c)表面的吸附研究探討。此表面上我們發現三個特殊的吸附位置。圖 1 展示可能的活性吸附位置，其中 Al_{III} 與 Al_{IV} 表示這些位置的可能配位數，因此有兩個配位數為 4 的吸附位置，以及一個配位數為 3 的吸附位置。表 1 列出了 CO 吸附於不同活性位置的吸附能量計算結果，並與 VASP 的計算作一比較[10]。
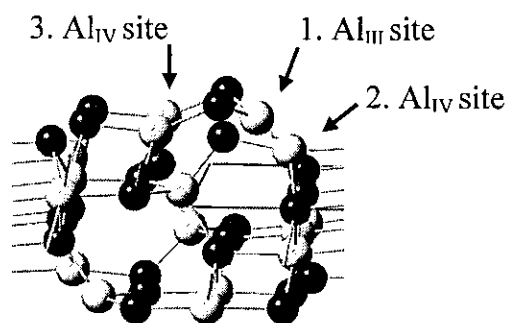
3. Al$_{IV}$ site   1. Al$_{III}$ site

2. Al$_{IV}$ site

Figure 1

Table 1. Comparison of the adsorption energy in different calculated sites

Site	1. Al$_{III}$ site	2. Al$_{IV}$ site	3. Al$_{IV}$ site
STO-3G	191	157	132
3-21G	168	141	122
6-31G*//3-21G	83	77	49
Kim [1,2]	72	40	17

Unit in kJ/mol

表 2 列出了 PBC-DFT 與 VASP 的分子結構參數計算值。圖 2 比較了 PBC-DFT 與 VASP 所計算的幾何結構差異。計算結果發現,以 3-21G 所得到的幾何結構相當接近由 VASP 所計算的結果,包含了吸附能與鍵長的計算。在相似吸附物結構中 (1),以 3-21G 所得的 Al-CO 距離與 VASP 的結果十分接近。VASP 與 3-21G 的鍵長(Al-CO)計算的差異僅約~0.004Å,而與 STO-3G 的差異則有 0.0308Å。在 CO 的頻率計算上,我們發現到 2143 cm^{-1} > 6-31g*、 2126 cm^{-1} > mp2、2113 cm^{-1} > VASP、2105 cm^{-1} > 3-21g、2004 cm^{-1} ~ STO-3G。這指出了在頻率的計算上,3-21G 也許比 VASP 具有更多的細節。

Table 2. Comparison of the detailed structure for 1. Al_{III} site

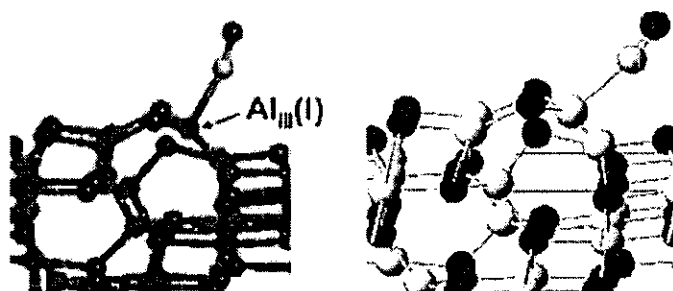|	D(Al--CO)	D(CO)	Δ bond	Free CO
Kim [1,2]	2.1360	1.137	-0.0083 ′	1.1453
3-21G	2.1401	1.155	-0.0087 ′	1.1639
STO-3G	2.1668	1.236	0.0323 ′	1.2044

Figure 2

在 H_2O 吸附中,我們以相似的方式完成了 PBC-DFT 的計算。不同於 CO 的吸附計算,其吸附能對基底函數有著相當大的相關性。

Table 3. Comparison of the adsorption energy in the different number of H_2O

nH_2O	Digne [3]	STO-3G	6-31G*//3-21G
1	240	390.8	214.2
2	191	534.7	282.2
3	141	378.8	190.6
4	88.0	252.7	135.1

Unit in kJ/mol

最近的 XRD 實驗發現[11-12]在 $x = 0.5$ 且 $y \sim 0$ 時,$Ce_{1-x}Zr_xO_{2-y}$ 具有最大量的表面。因此,我們以 $Ce_{0.5}Zr_{0.5}O_2$ (111) 表面為起點開始 VASP 的計算。由圖 3 的計算結果可以發現,由於陽離子半徑的差異造成晶格的扭曲,因而產生數個讓 Rh
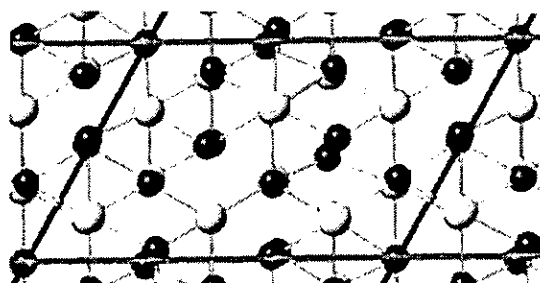
原子摻入的活性位置。我們也同時計算了 Rh 原子在這些可能
反應位置的吸附能量。這些結果列於表 4 之中。

Figure 2

Sites	Ce	Od	Ou	Zr Od
Ads. Energy /eV	-323.14	-324.48	-324.66	-324.89

Table 4

Rh 吸附發生時的最穩定結構是在當較下方的兩個氧位置
形成架橋型態的鍵結結構。我們目前已經計算了乙醇在包含了
1 到 2 個 Rh 原子的表面的分解反應。

5.建議

因為VASP需要大量的計算資源，所以我們十分緊迫的需
要在INER新的電腦叢集上執行計算工作，以完成乙醇在Al_2O_3
與$Ce_{0.5}Zr_{0.5}O_2$表面上的反應機構計算。

(三) J. C. Jiang（江志強）：

The interaction of Cu and Cu cluster with the α-Al_2O_3 (0001)
surface has been investigated using a periodic supercell approach.
All calculations have been undertaken within the molecular
dynamics and density functional theory. The structural

identification was determined via the simulation of X-ray powder diffraction, and structure parameters of α-Al₂O₃ were refined by the Rietveld method from simulated X-ray diffraction data. The simulation of x-ray diffraction as depicted in Figure 1 is showed

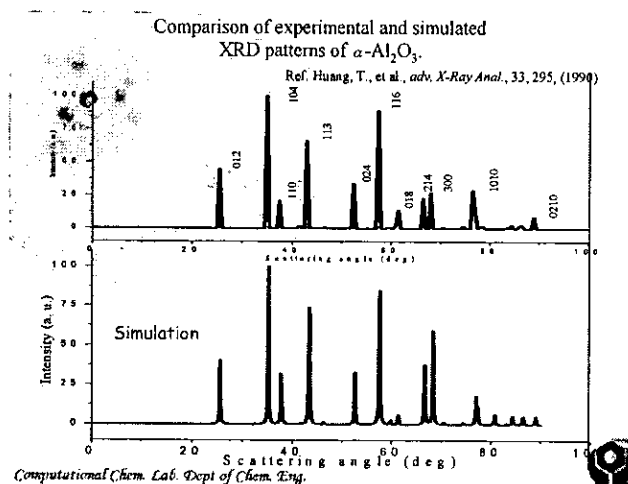Figure 1. The comparison of experimental and simulated XRD of α-Al₂O₃ powder.

in good agreement with previous experimental result by Huang, T et al. [13]. As shown in Figure 2, the α-Al₂O₃ (0001) surface, cleaved based on the bulk of MD structure, exists two hollow sites. As far to the study of Cu atoms deposition, our MD calculations
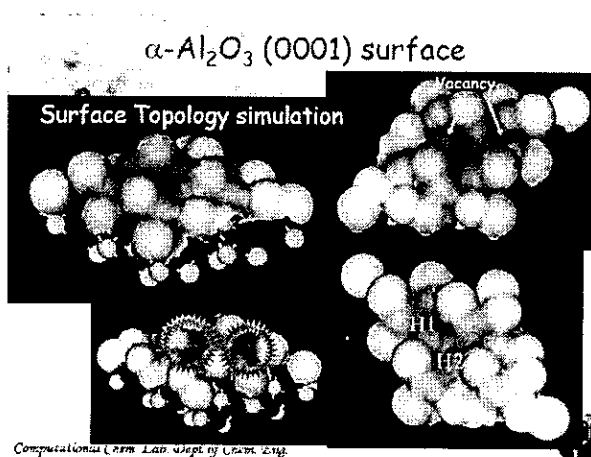

Figure 2. The MD-optimized structure of α-Al₂O₃ (0001) surface.

yielded trajectories for the deposition of Cu clusters on the α-Al$_2$O$_3$ (0001) surface. The result, as shown in Figure 3, indicates the formation of 3D clusters would take place, and

Top view and side view of the MD optimized Cu/Al$_2$O$_3$(0001) surface
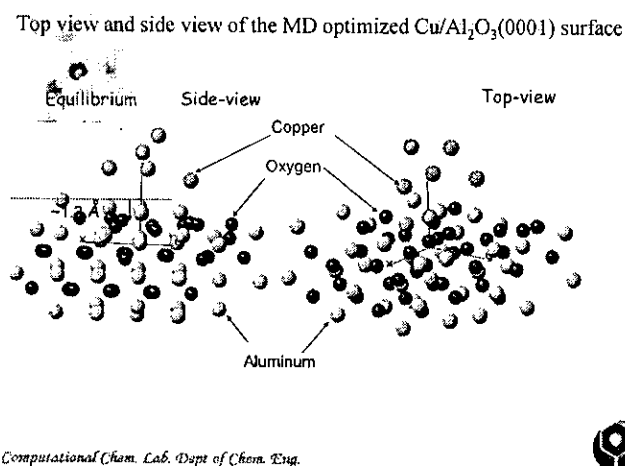
Figure 3. The MD-optimized structure of Cu$_6$/α-Al$_2$O$_3$ (0001) surface

hollow sites are energetically favorable for Cu cluster deposition. The preferred surface sites are those in which Cu atoms are close

Table 1. Some MD-optimized structural parameters of Cu$_6$/α-Al$_2$O$_3$ (0001) surface

Atom type	Simulated	Literatures
Cu - Cu	2.55 ~ 2.61 Å	2.54 Å [a]
Cu - O	1.74 ~ 2.03 Å	1.63 ~ 1.96 Å [b]
Cu - Al	1.59 ± 0.04 Å	1.58 Å [c]

[a] ref. 14; [b] ref. 15; [c] ref. 16.

to oxygen atoms (Table 1). Moreover, the analysis of local density of states by DFT calculations is used to explain the interaction between Cu cluster and the α-Al$_2$O$_3$ (0001) surface. Figure 4 shows the DOS of Cu cluster. Our results indicate that the
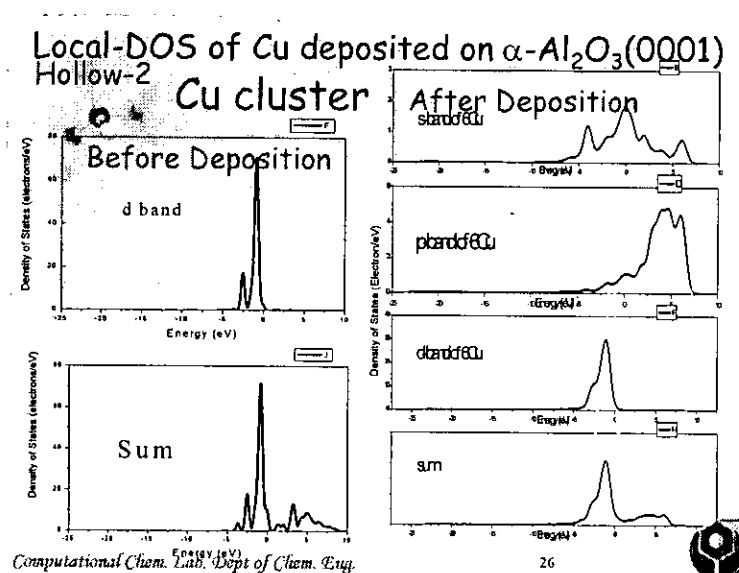
Figure 4. GGA density of states for Cu_6/α-Al_2O_3 (0001) surface. Left: DOS of isolate Cu cluster; right: after absorption projected on Cu_6.

(including the DOS projected on Cu cluster and oxygen atoms) electron density on Cu cluster (d- band) is reduced, whereas, that on oxygen (p-band) is increased. The analysis of Cu-cluster size effect is on the progress.

According to the study the reaction mechanism ethanol on α-Al_2O_3 [0001] surface without and with Cu metal deposition, the scope of this year includes: determination of surface termination based on surface energy, calculation of absorbed sites and calculation of energy barriers of the favorable reaction pathway. Except the last issue, we have completed the study of surface termination and absorbed sites.

二、量子點/二氧化鈦系統計算：

(一) J. S. Lin（林志興）：

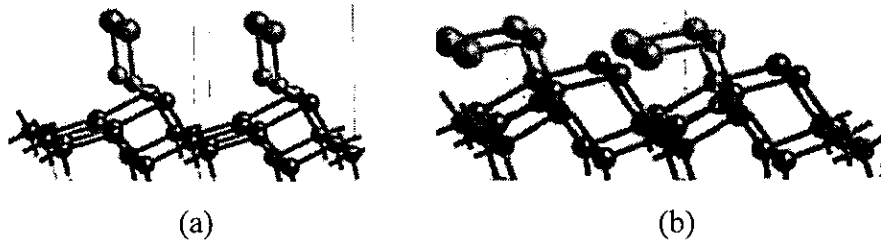1. InN 單層吸附於 Anatase(101)的組態與 InN/TiO$_2$ 介面電子結構：

對於InN單層吸附於Anatase (101)表面的吸附結構、態密度分部與光電激發能隙大小，在我們發表於JPCB的論文[17]中有詳盡的討論，兩種可能的單層吸附模式中以(Ocn2)2-InN-Ticn5 side-on模式較為穩定(參照表一)，而這兩種模式的光電激發能隙皆相較於Anatase的能隙3.2eV紅位移到UV/vis範圍。圖一(a)與(b)分別為計算的InN-Ocn2 end-on與(Ocn2)2-InN-Ticn5 side-on模式的吸附結構。(Ocn2)2-InN-Ticn5 side-on模式在費米能階上與最低能量傳導帶附近上吸附的InN、TiO$_2$表面與塊材有相當顯著的電子能態重疊，因此我們認為(Ocn2)2-InN-Ticn5 side-on模式較InN-Ocn2end-on模式更有助於InN/TiO$_2$介面激發電子注入TiO$_2$半導體過程的發生。

表一、InN 單層吸附與多層吸附於Anatase(101)的吸附能、能隙與多層吸附InN 的厚度

Monolayer-adsorbed InN on Anatase(101)	Adsorption Energy(eV)	Band gap(eV)	
InN-O$_{cn2}$ end-on	2.52	1.7	
(O$_{cn2}$)$_2$-InN-Ti$_{cn5}$ side-on	3.05	2.3	
Multilayer-adsorbed (InN)$_x$ on Anatase(101)			Thickness (Å)
Doublelayer-adsorbed InN	3.06	2.6	2.0
Triplelayer-adsorbed InN	3.18	1.4	4.0
Quadruplelayer-adsorbed InN		1.8	5.8

<div style="text-align: center;">(a)   (b)</div>

圖一、(a) InN-Ocn2 end-on 單層吸附模式與(b)(Ocn2)2-InN-Ticn5 side-on 單層吸附模式。其中藍色為N 原子、桃紅色為In 原子、紅色為O 原子、紫色為Ti 原子。

2. InN 多層吸附於 Anatase(101)的組態與 InN/TiO$_2$ 介面電子結構：

我們在JPCB的論文[17]中也報導了InN吸附於Anatase (101) 的雙層結構，這個結構是基於最穩定的(Ocn2)2-InN-Ticn5 side-on模式參考InN Würtzite晶體的堆疊方式所計算出來的。計算結果發現此雙層吸附模式的能隙相較於單層的 (Ocn2)2-InN-Ticn5 side-on模式略為紅位移至2.6eV (477nm)，態密度的分析顯示在費米能階上與最低能量傳導帶附近上吸附的InN、TiO$_2$表面與塊材仍然有顯著的電子能態重疊，因此吸附的InN雙層與TiO$_2$表面之間仍然存在相當程度的交互作用。為了更清楚地了解多層InN吸附所帶來的效應，我們根據此雙層吸附結構進一步建立了三層、四層InN的吸附計算，其結構請參照圖二。表一中列出了我們所計算的多層吸附InN之吸附能、能隙大小與吸附的多層InN的厚度。我們觀察到多層吸附的InN採取類似於InN Würtzite (110)表面的堆疊方式形成穩定的吸附，隨著吸附InN層數的增加，光電激發所需的能隙大致上持續地有紅位移的趨勢，然而我們觀察到此趨勢似乎具

<div style="text-align: center;">22</div>

有單數與奇數的區別，我們認為這可能是InN與TiO$_2$間存在晶格度不匹配所致。此外，從部分態密度的分析我們也發現單層與雙層InN吸附的光電激發能隙大小是由吸附的InN與TiO$_2$的電子能態來決定的，然而大於等於三層以上是由吸附的InN多層來主導光電激發能隙的大小(見圖三以雙層及三層InN吸附的部分態密度分析)。

(a)　　　　　　　　(b)　　　　　　　　(c)
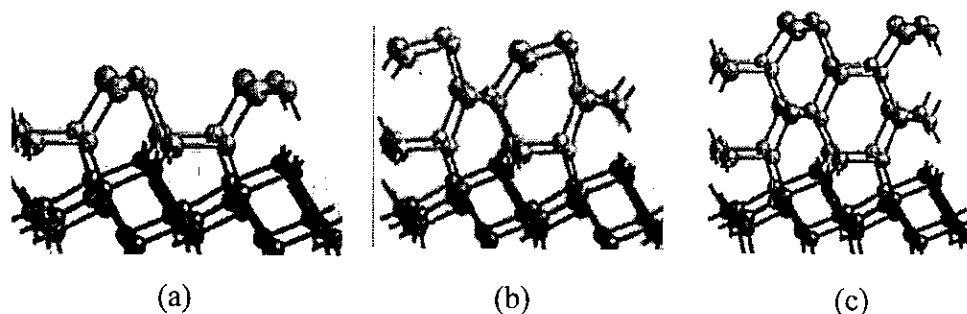
圖二、(a)雙層吸附模式(Doublelayer-adsorbed InN) (b)三層吸附模式(Triplelayer-adsorbed InN) (c) 四層吸附模式(Quadruplelayer-adsorbed InN)。

(a)　　　　　　　　　　　　(b)
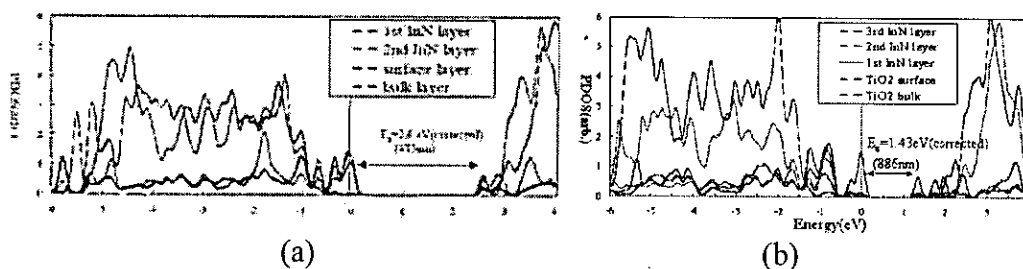
圖三、(a)InN雙層吸附模式的部分態密度分析，吸附的InN與TiO$_2$表面與塊材的電子能態於能隙邊緣有顯著的重疊；然而在InN三層吸附模式的態密度分析(b)中此能態重疊則逐漸消失。

3. InN 單層吸附於 Rutile (110)的組態與 InN/TiO$_2$ 介面電子結構：

在InN吸附於Rutile (110)表面的研究方面，我們的計算結果找到了三種可能的單層吸附模式，分別是 InN-Ticn5

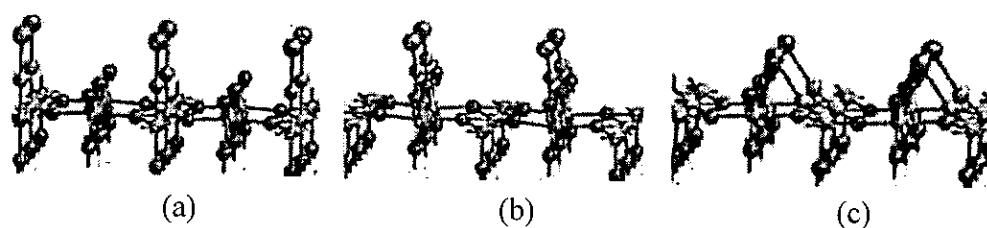end-on、InN-Ocn2 chain-like與Ocn2-InN-(Ticn5)2 side-on模式，其吸附結構請參照圖四。與吸附於Anatase(101)相似的是，以Ocn2-InN-(Ticn5)2 side-on模式明顯較為穩定(參照表二)，而這三種模式的光電激發能隙分別為1.5eV(837nm)、1.1eV(1127nm)與2.7eV(466nm)，皆使得吸收波長相較於Rutile的能隙3.0eV紅位移到UV/vis範圍。InN-Ocn2 chain-like與Ocn2-InN-(Ticn5)2 side-on模式在費米能階上與最低能量傳導帶附近上吸附的InN、TiO_2表面與塊材皆有部分的電子能態重疊，因此我們認為相對而言InN-Ticn5 end-on模式是較不利於激發電子注入TiO_2半導體過程的發生。

(a)   (b)   (c)

圖四、(a) InN-Ticn5 end-on 吸附模式(b) InN-Ocn2 chain-like吸附模式與(c) Ocn2-InN-(Ticn5)2 side-on 吸附模式。

表二、InN 單層吸附與多層吸附於Rutile(110)的吸附能、能隙與多層吸附 InN 的厚度。

Monolayer-adsorbed InN on Rutile(110)	Adsorption Energy(eV)	Band gap(eV)	
InN-Ti$_{cn5}$ end-on	1.65	1.5	
InN-O$_{cn2}$ chain-like	2.65	1.1	
O$_{cn2}$-InN-(Ti$_{cn5}$)$_2$ side-on	4.35	2.7	
Multilayer-adsorbed (InN)$_x$ on Rutile(110)			Thickness (A)
Doublelayer-adsorbed InN, mode-1	2.95	1.2	2.7
Doublelayer-adsorbed InN, mode-2	3.89	1.8	4.9
Doublelayer-adsorbed InN, mode-3	1.34	—	6.1
Triplelayer-adsorbed InN	3.76	1.3	8.4

4. InN 多層吸附於 Rutile (110)的組態與 InN/TiO$_2$ 介面電子結構:

我們根據最穩定的Ocn2-InN-(Ticn5)2 side-on 單層吸附模式計算出了兩種雙層吸附模式,分別稱為doublelayer mode-1與doublelayer mode-2。而這兩種雙層吸附模式的能隙相較於Ocn2-InN-(Ticn5)2 side-on單層吸附模式分別紅位移至1.2eV(1033nm)與1.8eV(696nm),且吸附能顯示皆為相當穩定的吸附模式(參照表二)。其次,根據InN-Ocn2 chain-like單層吸附模式我們也計算出了第三種雙層吸附模式,稱為doublelayer mode-3,然而此模式的吸附能說明了這種雙層吸附模式並不穩定。最後我們根據doublelayer mode-2計算出三層InN吸附的結構,圖五為三種雙層模式與三層模式的計算結構。我們觀察到隨著吸附InN層數的增加 (Ocn2-InN-(Ticn5)2 side-on Doublelayer mode-2 Triplelayer),光電激發所需的能隙發生持續紅位移的趨勢,這樣的趨勢相較於多層InN在Anatase(101)上的吸附較為單純。多層InN 在Rutile (110)吸附的費米能階上主要為吸附的InN的電子能態,然而與Anatase(101)不同的是在最低能量傳導帶附近上出現了多層InN、TiO$_2$表面與塊材三者電子能態的重疊,這可能代表多層InN 在Rutile(110)吸附模式可能存在與多層InN在Anatase(101)吸附模式不同的激發電子注入InN/TiO$_2$介面途徑。最後,我們將所有計算出的吸附模式之能隙與UV 吸收波長與林院士研究群的InN量子點吸附在TiO$_2$奈米粒子的UV 光譜實驗結果[2]對照,請見圖七。

(a)   (b)

(c)   (d)
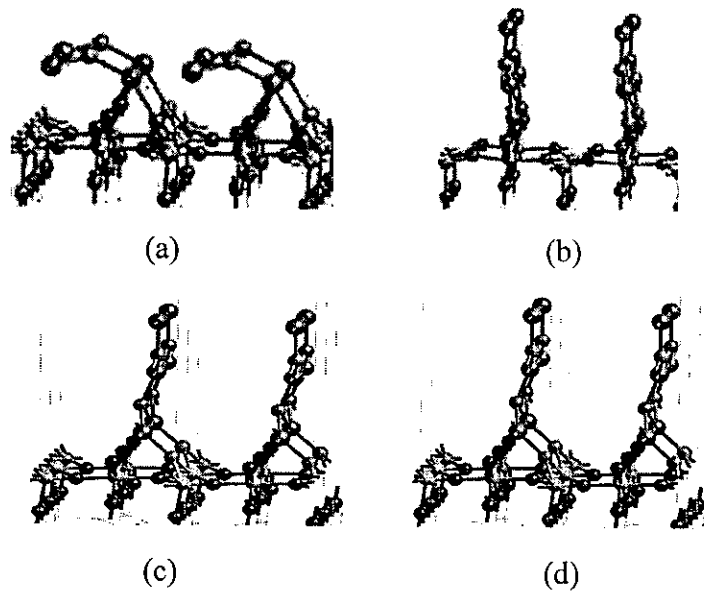
圖五、(a) InN雙層吸附模式一(doublelayermode-1)、(b) InN雙層吸附模式
二(doublelayermode-2)、(c) InN雙層吸附模式三(doublelayermode-3)與(d)
InN三層吸附模式(triplelayer)
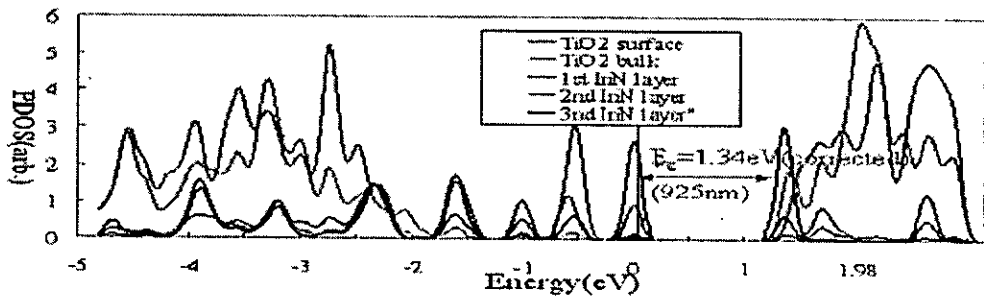
圖六、InN 三層吸附模式的部分態密度分析。

(a)   (b)
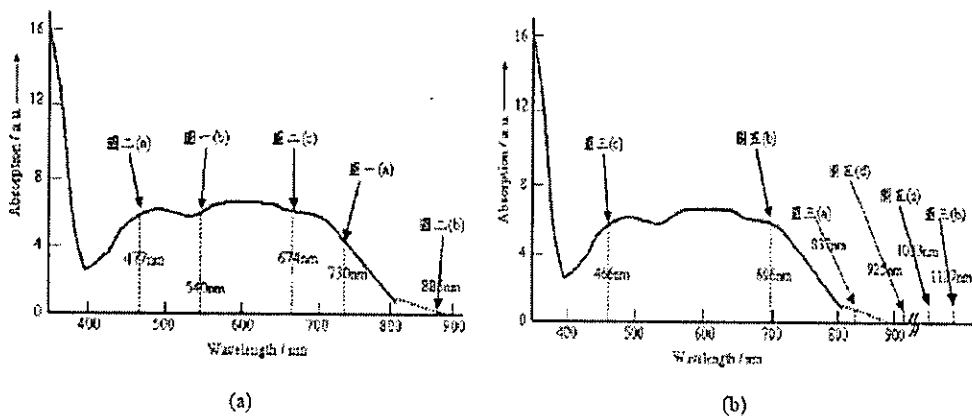
圖七、褐色曲線為實驗UV吸收光譜，分別對照(a) (InN)ₓ 在 Anatase(101)表面的各種吸附模式及(b) (InN)ₓ 在
Anatase(101)表面的各種吸附模式所需的光電激發能隙之吸收波長，相對應的吸附模式請參照紅色符號上方
的圖片號碼標示。

26

(二) B. C. Wang（王伯昌）：

目前就一般矽量子點而言，其原子數目仍然遠多於計算效能的合理範圍。從理論的觀點來說，若是要滿足實際的狀況，幾乎是不可能的任務，因此通常只計算一系列結構中的最小結構，然後不斷的增加其計算的片斷到可以計算的極限，最後將這一系列的結果數據作回歸分析，若其計算結果和分子大小成線性關係的話，則可以用此縮小模型估計實際分子大小的性質與行為。雖然這樣的作法仍有估計風險存在，但在有限的資源下，這樣的方式仍為一個不錯的解決方法。矽量子點的幾何結構有可能為 T_d 結構或者其他結構。理論上，T_d 結構的氫化矽量子點有著類似鑽石鍵結的球型結構，而在其外圍加上氫原子以消除未連結鍵結的部份，一般而言對於未鍵結的處理通常都是加上氫原子，以免不正常存在的自由電子造成計算上的錯誤。

1. 計算方法：

在計算方法的部份，在較小尺寸的矽量子點部分，我們採用了 Gaussian 03 軟體所提供的 AM1、PM3 半經驗方及密度泛函數理論中的 B3LYP/6-31G*做計算。對於較大尺寸的矽量子點來說，Gaussian 03 計算資源難以負荷，於是我們採用 SIESTA 方法，搭配 double-ξpolarized orbitals 的基底函數，最佳化後的結果再以，軟體中的 AM1、PM3、B3LYP/6-31G*等方法，做電子結構的單點計算。

2. 結果與討論：

計算 T_d 結構的矽量子點能隙，結果如下表一(單位 eV)。

Compounds	LDA / SIESTA	B3LYP // SIESTA	AM1 // SIESTA	PM3 // SIESTA	B3LYP /6-31G*	AM1	PM3
Si_5H_{12}	5.96	7.65	9.31	7.3	7.6	9.21	7.28
$Si_{17}H_{36}$	4.42	5.98	8.32	6.08	5.76	8.28	6.09
$Si_{29}H_{36}$	3.67	5.32	7.85	5.6	5.29	7.84	5.59
$Si_{35}H_{36}$	3.56	5.12	7.73	5.43	5.1	7.71	5.41
$Si_{47}H_{60}$	3.4	4.94	7.62	5.25		7.62	5.04
$Si_{71}H_{108}$	2.75	4.18	7.24	4.94		7.22	4.96
$Si_{99}H_{100}$	2.52	3.95	7.03	4.66		7.02	4.66
$Si_{147}H_{148}$	2.22	3.62	6.87	4.42			
$Si_{281}H_{172}$	1.69	3.06	6.58	4.06			

由上表中我們可以發現，隨著矽量子點的直徑增加而能隙會減小。而半經驗方法也許是因為對於較複雜的雙原子間的重疊積分項直接帶入經驗值加以簡化，導致所得的能隙皆比密度泛函數理論計算所得的能隙高。至於 SIESTA 所計算的能隙會偏低，是因為採用局域密度近似(LDA)方法所導致。接著我們用 -CH$_3$、-OH、-NH$_2$、-OCH$_3$ 等等的取代基替換掉外圍的氫原子，使用 T_d 結構 Si35 大小的矽量子點，所得到的能隙結果如下表二(單位 eV)。

Compounds	B3LYP/SIESTA			LDA/ SIESTA
	HOMO	LUMO	Energy Gap	
$Si_{35}H_{36}$	-6.80	-1.68	5.12	3.56
$Si_{35}(CH_3)_{36}$	-5.43	-0.83	4.60	3.13
$Si_{35}(OH)_{36}$	-5.60	-2.75	2.84	1.48
$Si_{35}(NH_2)_{36}$	-4.13	-0.74	3.39	2.05
$Si_{35}(OCH_3)_{36}$	-5.66	-2.43	3.23	1.67
$Si_{35}(CH_2CH_3)_{36}$	-5.34	-0.75	4.59	3.09

由表二結果可以發現，若矽量子點外圍接推電子基團，則會降低矽量子點的能隙。

3. 結論：

在我們的計算結果中，使用 B3LYP/6-31G*和 B3LYP // SIESTA 所計算的結果相當接近，同樣在半經驗方法 AM1 與 AM1//SIESTA 的能隙計算結果也相當接近。PM3 和 PM3 // SIESTA 也是類似的結果。在不同的取代基效應上，若是將外圍的氫換成-CH₃ 或-CH₂CH₃ 對矽量子點能隙影響不大。若是將外圍的氫置換為-OH 或-NH₂、-OCH₃，則矽量子點的能隙會降低很多。這可能是因為推電子基改變了矽量子點的電子結構而導致。由以上結果我們認為 B3LYP/6-31G*與 B3LYP//SIESTA 這兩種全始算的密度泛函理論計算結果，可以用在預測矽量子點的能隙上。所以我們提出先以 SIESTA 軟體對矽量子點作幾何結構最佳化，再以此結構用 Gaussian 03 軟體作單點計算，稱之為 B3LYP // SIESTA 方法來作為研究矽量子點的電子結構，不但可以節省計算時間，也可以計算更大的矽量子點結構。

(三) Y. R. Tzeng and M. C. Lin（曾怡仁、林明璋）：

We calculated the site projected density of state (DOS) for the hydrogen terminated Si quantum dots (QDs) chemisorbed on the anatase-TiO_2 (101) surfaces using the Vienna ab-initio simulation package (VASP).

As show in Figure 1(a), the adsorption of SiH_2 has the effect of filling the electron into the conduction band of the TiO_2, and

thus modifies the electronic property of the anatase-TiO_2 (101) surface from a semiconductor ($E_g \sim 2.4$ eV) to a conductor.

By keeping the Si atoms in their tetrahedral coordinates and increasing the size of Si QD to $Si_{35}H_{34}$, we found the conducting property of TiO_2 surface remain unchanged. The increase in the Si QD size, as shown in Figure 1(c) and comparing it to the DOS of SiH_2 in Fig. 1(b), mainly add several closely packed Si energy levels, located ~ 1.5 eV below the Fermi level. This effectively reduced the valence-conducting energy gap from 2.4 to 1.5 eV, allowing optical absorption in the visible light range.
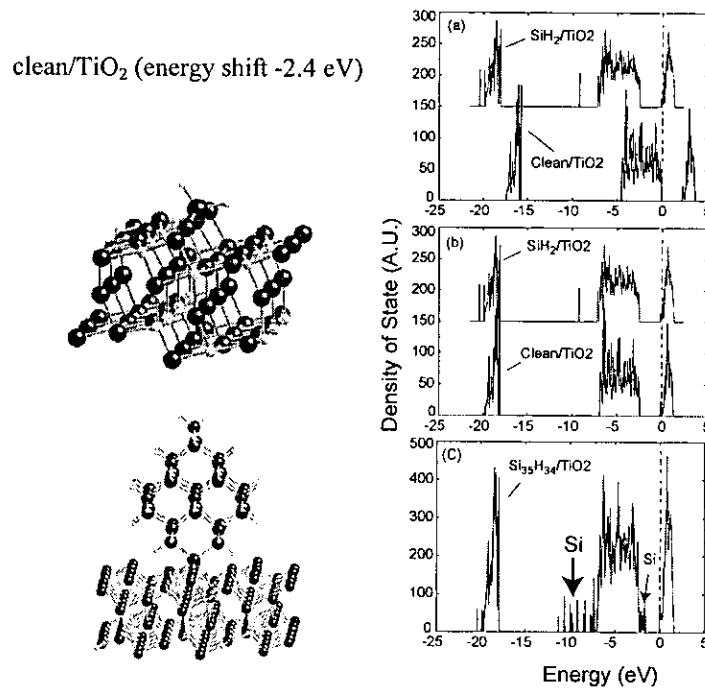
Figure 1. Optimized geometries and DOS of Si QDs

For the range of $Si_{n<=67}H_{x<=98}$ compositions, the effective energy gap ΔE (energy difference between the valance band of Si and the conduction band of TiO_2) as a function of the size of Si QD is shown in Figure 2.

Si-QD on the Anatase TiO$_2$(101) surface

Figure 2. Effective energy gap (E$_g$) of Si QDs as a function of Si numbers on the Anatase-TiO$_2$ (101) surface.

Due to the effect of the shift in Fermi energy level, there is a charge transfer from the SiQD to TiO$_2$ surface. As shown in Figure 3, the transferred charge is spread to the conduction band located on the Ti sites.

Figure 3. Bader Charge Distribution of anatase-TiO$_2$ (101) surface

三、SCC-DFTB 程式研發（Henryk Witek）：

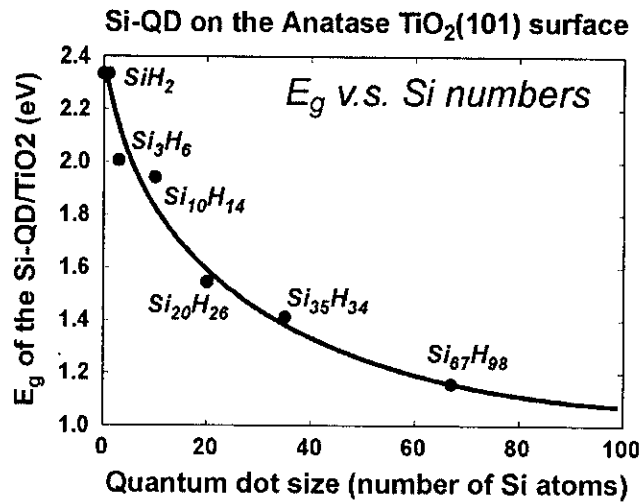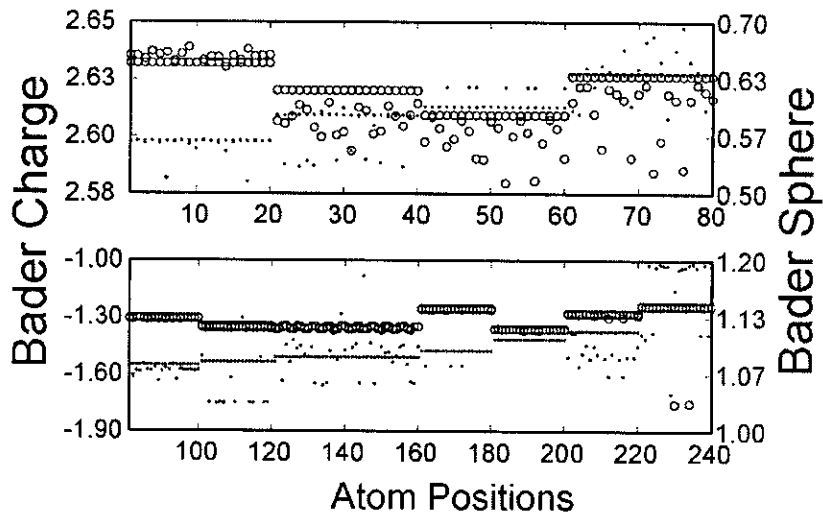The self-consistent charge density-functional tight-binding (SCC-DFTB) method[18-19] is a semiempirical computational technique that allows for fast and rather reliable determination of molecular structures, energetics, and vibrational spectra of medium and large-size molecular systems. It considers explicitly only valence electrons and therefore, allows for substantially larger size of eigenvalue problems than standard ab initio methods. The accuracy of SCC-DFTB is rather striking in comparison with other related approaches like BLYP/cc-pVDZ or B3LYP/cc-pVDZ; at the same time the computational effort is reduced substantially even by a few orders of magnitude. SCC-DFTB and other related approaches, like DFTB[20] and spin-polarized SCC-DFTB[19], were applied over the last two decades for simulations of various chemical and physical properties of large number of molecules and materials. In particular, they were used for modeling surface properties and characteristics of crystals and clusters containing gallium, arsenic, nitrogen, silicon, carbon, boron, and aluminum. They were also used to study properties of some semiconductors. Another very important field of applications of SCC-DFTB is the chemistry of biomolecules. DFTB was used for a number of publications investigating the dynamics and structure of small crystalline and amorphous carbon clusters. Another field of applications of SCC-DFTB is computational spectroscopy. This method was used to a number of studies investigating the infrared and Raman spectra of various carbon nanomaterials,[21-22] starting from fullerenes and ranging up to assemblies of fullerenes and

nanotubes. To this end, a dispersion correction was introduced in the SCC-DFTB formalism allowing for treating weak, long-range van der Waals interactions.

One of the largest practical drawbacks of SCC-DFTB is its limited applicability stemming from incomplete set of the parameter files. The existing parameterization of the SCC-DFTB method is limited to five elements: carbon, hydrogen, nitrogen, oxygen, and sulfur. For these elements, there exist a unified set of Slater-Koster files (that can be treated as a counterpart of electron basis sets in usual quantum chemistry programs) that allows for straightforward transferability of SCC-DFTB to a very wide class of molecules and materials containing those elements. There also exists a number of scattered Slater-Koster files for other pairs of elements (including gallium, boron, zinc, iron, copper, and a few others) that have been developed independently from the backbone CNOHS set and therefore it cannot be combined with the backbone set in one calculation. The main problem here is lack of correspondence of various atomic radii and confinement potentials used in these parameterizations. There is clearly an urgent need for reliable Slater-Koster files for a majority of elements across the periodic table of elements. Here, we report progress of our recent efforts to produce a set of such files.

The parameterization process of the SCC-DFTB method is divided in a number of stages. The initial stage is solving atomic DFT problem that would produce atomic densities, atomic exchange-correlation potentials, and a set of valence orbitals. This step requires numerical integration of radial atomic Kohn-Sham

problem. We have chosen to solve a four component Dirac-Kohn-Sham problem. In relativistic regime, the radial equation can be reduced to a set of coupled differential equations for the f and g radial wave functions. A solution to this problem is sought following Desclaux.[23] We have adapted the classical program of Desclaux (in practice it meant a complete rewriting the program due to completely changed standard of FORTRAN programming); new, more accurate exchange-correlation potentials replaced the original $X\alpha$ potential of Slater. The adapted program was also modified in a large part to allow for employing various ideas and concepts commonly used in nowadays quantum chemistry programs. One of such modifications was introducing a functional representation of calculated potentials and spinors for functions that in the original code are represented on a numerical grid. This approach gives us many benefits since it allows for accurate generation of atomic densities and orbitals without usual finite basis set limitations.

Next stage of the parameterization process was writing a program to calculate two-center integrals from the previously calculated atomic orbitals and corresponding atomic densities. Currently, this step is not yet completed but should be finished within the next few months. We have derived all necessary equations and constructed the main part of the code; however, the code requires serious enhancements and debugging in order to ensure correct results. This is a very crucial and error-prone step. It requires frequent justifications and exact control of the intermediate quantities in order to avoid numerical and algorithm errors.

Development of this part of code is the main part of our current scientific activity.

Next stage of the SCC-DFTB parameterization process is computing repulsive, two-center core-core potentials. These potentials are meant to account for the atomic nuclei and core electron interactions. An assumption of energetic separability of such interactions is well justified through some theoretical arguments and through actual calculations; presently employed form of these interactions—namely sum of two-center potentials over all possible atomic pairs in a molecule—seems to work accurately for all tested systems. Usually, such potentials are obtained from auxiliary DFT calculations performed for a chosen group of chemicals over a broad range of distances. We have
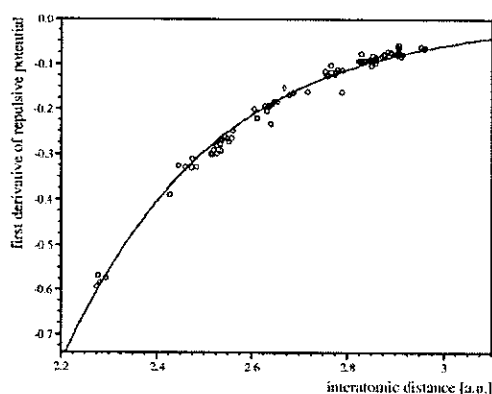

Fig.1. First derivative of repulsive carbon-carbon potential derived from experimental equilibrium geometries for a large group of hydrocarbons. Dots denote experimental data and the line, an analytical fit.

shown that this scheme not necessarily leads to best agreement with experimental findings. An alternative scheme has been proposed, where the repulsive potentials are obtained directly from experimental data. We showed that this new scheme can reproduce the geometrical and vibrational parameters with better accuracy

than corresponding DFT results. [24] Presently, we are working [25] on unifying the potential optimization approach in a way that includes also the reaction energetics in the optimization process. The new scheme described here allows for obtaining much better accuracy with the SCC-DFTB method and can be in practice applied to any pair of elements providing that a sufficient experimental data is provided. For elements where no sufficient data are available, an alternative approach can be used where the repulsive potentials are fitted to the results of accurate quantum chemical calculations employing either multireference CI or multireference perturbation theory.

Discussion: Development of full set of Slater-Koster files is of a great importance for the DFTB community. Presently, a new set of parameters is developed anew for each research project; this set is meant to reproduce well all the physical and chemical quantities that a given project is supposed to reproduce. This paradigm leads very often to a situation where many Slater-Koster files exist for some pair for elements and there is no clear answer if they can be used for reproducing other properties. Our project is meant to yield an universal set of parameters that can be used for molecular structure calculations and that is supposed to reproduce well energetics, equilibrium structures, and vibrational properties of molecular systems ranging from small, few atom structures through clusters to crystalline and amorphous surfaces. The progress reported in present report shows that efforts toward achieving this aim are already very advanced and we can soon start producing all necessary sets of Slater-Koster files that can be

universally transferred to virtually any molecular system.

Resulting publications:

1. B. Trzaskowski, H. Witek, A. Jalbout, E. Malolepsza, K. Morokuma, L. Adamowicz, "Encapsulation of C_{60} Fullerenes by Carbon Nanotubes; a Theoretical Analysis", *Chem. Phys. Lett.*, submitted

2. H. Witek, S. Irle, G. Zheng, B. de Jong, and K. Morokuma, „Modeling carbon nanostructures with the self-consistent charge density-functional tight-binding method: Vibrational and electronic spectra of C_{28}, C_{60}, and C_{70}", J. Chem. Phys. **125** (2006), in press

3. Ch. Mou and H. Witek, "Modeling internal rotation and bending potentials using the SCC-DFTB method", in preparation

4. E. Malolepsza and H. Witek, "Optimal repulsive potentials for the SCC-DFTB method", in preparation

5. H. Witek, "Relativistic parameterization of SCC-DFTB method", to be submitted to J. Phys. Chem. A

四、TMIn 與水及硫化氫的反應（Raghu Putikam and M. C. Lin）：

We have carried out studies on the reactions of $In(CH_3)_3$ with H_2O and H_2S with the geometry optimization of all the reactants, products, transition states, and intermediate molecules in their ground state configurations using the G03w program. The optimizations are carried out on all of the possible reactions between the Trimethylindium (TMIn) with H_2O and H_2S by the B3LYP and MP2 methods. The B3LYP functional consists of Becke's three-parameter hybrid exchange functional combined with

the Lee-Yang-Parr correlation functional. Heat of formation ($\Delta H_f^\circ{}_0$) for the Indium oxide (InO) and Indium sulfide (InS) are calculated using the CCSD (T)/Lanl2dz//B3LYP/Lanl2dz level.

1. Reactions of Trimethylindium $(CH_3)_3In$ with H_2O:

Trimethyl indium has a planar C_{3h} symmetry, and the bond length of In-C is 2.157 Å with low-barrier rotation for the methyl groups. The association reaction of the electron deficient $In(CH_3)_3$ and H_2O can form two van der Waals complexs, i.e. $[(CH_3)_3In:OH_2$ (R1)] and $[(CH_3)_2InCH_3:HOH$ (R2)] as shown in Figure 1. Complexation with a molecule of water yields a most stable complex structure, R1, which lies 15.2 kcal/mol and 16.0 kcal/mol below the reactants calculated at the B3LYP/LanL2dz and MP2/lanl2dz methods respectively. The predicted value is 17.8 kcal/mol, by both CCSD(T)//B3LYP and CCSD(T)//MP2 methods. As shown in the Figure 1, water is located with oxygen pointing towards the In atom in the top and middle of molecule at a distance of 2.294 Å (2.319 Å by MP2). The complex has C_1 symmetry, and the C-In-C angle has changed from 120° to 118°. Formation of second complex, R2, is very weak and has only 2.1 kcal/mol binding energy. Hydrogen of water interacts with one of the CH_3 of $In(CH_3)_3$ with an H-C bond length of 2.484 Å by the DFT method and 2.615 Å by the ab initio method. The geometry of the $In(CH_3)_3$ fragment in the complex shows very little change in one of the In-C bond length 2.265 Å (compared to isolated $In(CH_3)_3$).

The decomposition of R1 to the most stable intermediate $(CH_3)_2InOH$ and a CH_4 molecule requires the transition state

energy at TS1 of around 22.5 kcal/mol (or 4.7 kcal/mol above the reactants). The transition vector is dominated by the motion of hydrogen, which is 1.160 Å from the oxygen and 1.515 Å from the carbon. The In-O bond is almost formed (2.106 Å vs 1.906 Å $(CH_3)_2InOH$). The In-C bond is substantially elongated to 2.412 Å from 2.157 Å in $(CH_3)_3In$. Based on the CCSD (T)/ LanL2dz //B3LYP/LanL2dz level potential energy calculation, the formation of the $(CH_3)_2InOH + CH_4$ products are found to be most exothermic 33.7 kcal. Calculations from the MP2 method also confirm the result with 33.2 kcal/mol exothermicity. Geometrical parameter of the $(CH_3)_2InOH$ molecule in terms of bond length between the In-O is 1.906 Å and In-C is 2.147 Å. On this surface, we were unable to locate the transition states for the decomposition and isomerization of the van der Waals complex $(CH_3)_2InCH_3:HOH$ (R2).

The decomposition of the $(CH_3)_2InOH$ product to $CH_3InO + CH_4$ requires 73.1 kcal/mol of energy; the decomposition takes place via the transition state (TS2) with O-H and In-C bond lengths of 1.323 Å and 2.550 Å respectively. TS2 is very similar to TS1, located at 30.5 kcal/mol and 33.6 kcal/mol above the association complex of TMIn + H_2O reactants calculated using the B3LYP/LanL2dz and MP2/Lanl2dz level respectively. The CCSD(T) energy calculated with both B3LYP and MP2 optimized geometries essentially the same around 39 kcal/mol. In this potential energy surface, the reaction channel producing $CH_3InO + 2CH_4$ is only 0.4 kcal/mol above the reactants. Further decomposition of CH_3InO produces the doublet radicals of InO

and CH_3. In this process, breaking of CH_3 from indium requires 46.5 kcal/mol of endothermic energy predicted at CCSD(T)//B3LYP method. Doublet electronic state of diatomic In-O bond length is 2.061 Å which is longer when compared to intermediate CH_3In-O (bond length of In-O is 1.801 Å) radical.

2. Reactions of Trimethylindium $(CH_3)_3In$ with H_2S:

In this section, we describe in detail the mechanism for the analogous H_2S reaction along the PES's and try to underline the similarities and differences between the two ligands. The calculated structures of intermediates, transition states and products of all investigated reactions are given in Figure 3 and relative energies are given in Table 1. The potential energy surface has been studied at the CCSD (T) /LanL2dz // B3LYP/LanL2dz level of theory and is presented in Figure 4. The predicted vibrational frequencies for all these species are summarized in Table 3. The relative energies are calculated with respect to the reactants, $In(CH_3)_3 + H_2S$.

The gas-phase association reaction of trimethylindium with hydrogen sulfide can give rise to two van der Waals complexes, $(CH_3)_3In:SH_2$ (R3) and $(CH_3)_2InCH_3:HSH$ (R4) without intrinsic barriers. Formation of the R3 is less exothermic when compared to R1 and has a value 6.5 kcal/mol below the reactants. First step in this reaction is sulphur atom interacting with indium of $In(CH_3)_3$ to give the R3 complex. The bond length of In-S is 3.141 Å and 3.134 Å calculated at the B3LYP/LanL2dz and MP2/Lanl2dz levels respectively. The hydrogen bonding energy

between the CH_3 -group and a hydrogen atom of the H_2S molecule was found to be 1.3 kcal/mol, which is less exothermic when compared to analogous H_2O complex, 2.1 kcal/mol.

Complex R3, $(CH_3)_3In:SH_2$ can decompose to give $(CH_3)_2InSH + CH_4$ by a cyclic transition state. This reaction channel is predicted to have a potential barrier of 23.3 kcal/mol, which may be compared with the value of 13.7 kcal/mol by B3LYP and 21.5 kcal/mol by MP2 methods. The exothermicity of the process is predicted to be 36.0 kcal/mol. The transition state (TS3) of this channel is nonplanar, and the reaction takes place with the formation of the In-S bond with a bond length of 2.881 Å and bond between the S-H and C-H is 1.615 Å and 1.575 Å respectively. The bond length of In-C elongates from 2.157 Å in TMIn to 2.334 Å. The intermediate product $(CH_3)_2InSH$ has the In-S bond length 2.479 Å and In-C bond length 2.139 Å according to the B3LYP methods; these values may be compared with 2.469 Å and 2.158 Å obtained by the MP2 method. From the $(CH_3)_2InSH$, the reaction proceeds by the migration of a hydrogen atom from S to C to eliminate CH_4 and the CH_3InS product via transition state TS4. The barrier height of this reaction is about 53.3 kcal/mol which may be compared with the values 45.9 kcal/mol and 51.4 kcal/mol calculated at B3LYP and MP2 methods respectively. In this PES, the formation of products $CH_3InS + 2CH_4$ is most exothermic with 36.7 kcal/mol exothermicity. In the $In(CH_3)_3 + H_2S$ reaction channel, the two intermediate products $(CH_3)_2InSH + CH_4$ and $CH_3InS + 2CH_4$ have almost same exothermic energy.

CH₃InS has C₃ᵥ symmetry with the In-S and In-C bond lengths predicted to be 2.244 Å and 2.114 Å respectively. Finally the dissociation of the most stable intermediate CH_3InS to doublet InS and CH_3 radicals is highly endothermic (49.7 kcal/mol). The final reaction product of this PES is InS + 2 CH_4 + CH_3 which is around 21.3 kcal/mol above the reactants predicted by B3LYP method and 13.0 kcal/mol by the CCSD(T)//B3LYP method. Here the energy difference between the two methods is 8.2 kcal/mol. In the quartet state of diatomic InS and InO, their bonds are very long and unstable. The InO and InS molecules have doublet ground state bond lengths of 2.061 Å (2.073 Å) and 2.608 Å (2.613 Å) respectively calculated by B3LYP (MP2) methods.
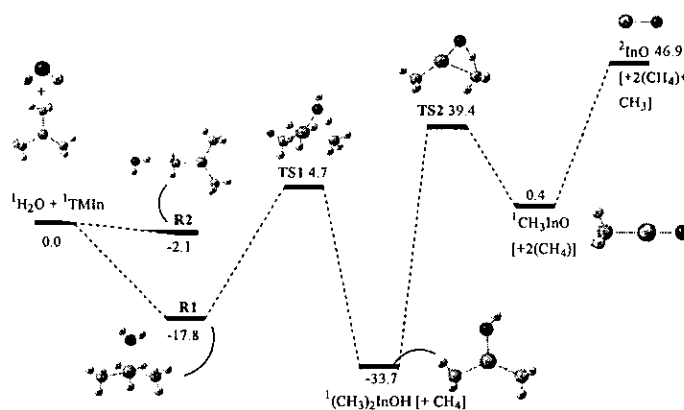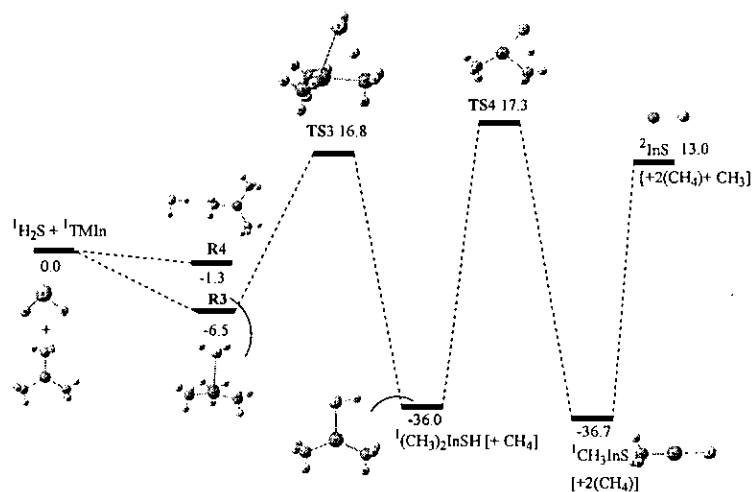
Figure 1

Figure 2

42

Figure: Potential Energy Surface of H_2O and H_2S with TMIn reactions. Relative energies (kcal/mol) calculated using CCSD(T) / LANL2DZ // B3LYP / LANL2DZ method.

Species	Reactions	Heat of reaction (0K) $\Delta_r H^0_0$	Heat of formation (0K) $\Delta_f H^0_0$
H_2O + TMIn reaction:			
R1	H_2O + TMIn→ **R1** (TMIn-OH_2)	-15.98	-20.13
DMInOH	R1 → DMInOH + CH_4	-16.50	-20.63
MInO	DMInOH → MInO + CH_4	33.68	29.04
InO	MInO → InO + CH_3	42.12	35.53 (88.72, 10.72, 37.7)
H_2S + TMIn reaction:			
R3	H_2S + TMIn→**R3**(TMIn-SH_2)	-5.17	43.60
DMInSH	R1 → DMInSH + CH_4	-27.81	31.786
MInS	DMInSH → MInS + CH_4	0.63	48.41
InS	MInS → InS + CH_3	45.67	58.45 (57.36)

Table: Heat of reaction and Formation of species (in kcal/mol) predicted at the CCSD (T)/Lanl2dz//B3LYP/lanl2dz level of theory.

The experimental values are obtained based on the heats of formation at 0 K for $(CH_3)_3In$=52.97 Kcal/mol (calculated from 298 K value using vibrational frequencies in this work; H_2O=-57.117 Kcal/mol; H_2S=-4.204 Kcal/mol; CH_4=-16.0±0.08 Kcal/mol; CH_3=35.86±0.07 Kcal/mol; Experimental values of InO and InS are given in parentheses.

五、乙醇轉氫的實驗 (J. F. Cho / C. S. Lee / M. C. Lin) ：

(一) Ethanol to H_2 conversion efficiency on Rh/CeO_2:

CeO_2 nanocrystals of cube and rod shape have been synthesized under hydrothermal conditions on controlling the pH, temperature and duration of reaction. High-resolution transmission

electron microscopy indicates that exposed crystal planes are {110} and {100} for rods but {100} for cubes. Figure 1a shows a SEM image of CeO_2 nanorods as prepared. The result indicates that most CeO_2 nanocrystals exhibit a rod shape with diameter and length in the ranges 20-30 and 100-200 nm respectively. The inset of Figure 1a presents a TEM image and a SAED pattern of a CeO_2 nanorod that reveals interplanar spacing 0.28(1) nm attributed to (200) and (020) planes, indicating preferred growth in the direction [110]. This result and other TEM images indicate that the CeO_2 cubes are enclosed with {110} and {100} planes, consistent with previous report on the synthesis of CeO_2 nanorod. The CeO_2 nanocubes as obtained had a regular cubic shape with a mean length 40 nm (Figure 1b). A TEM lattice image taken from a single CeO_2 cube clearly shows interplanar d-spacings 0.27(1) nm, which is near that of (002) planes of cubic CeO_2 (inset of Figure 1b). This result indicates that the CeO_2 cubes were enclosed with {100} planes. These nanocrystals have been used in the preparation of a Rh/CeO_2 catalyst (5 % mass of Rh) on an Al_2O_3 support to test the catalytic activity for ethanol reforming.
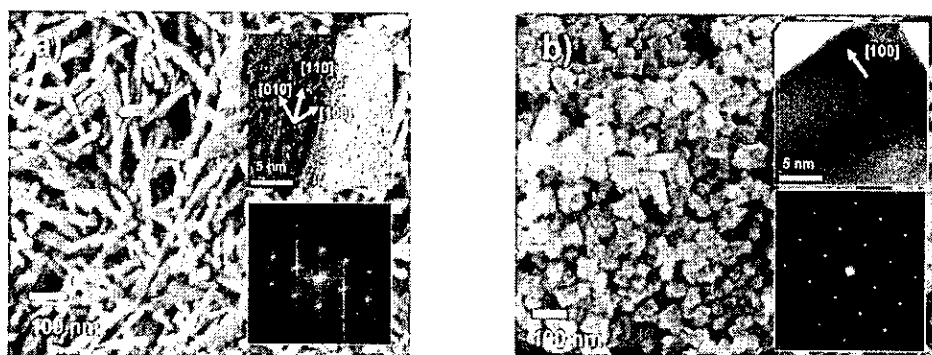

Figure 1. SEM images of CeO_2 nanorods (a) and nanocubes (b). The insets are TEM images and SAED patterns for a single rod and cube sample, respectively.

With GC-MS we investigated the effect of CeO_2 morphology on H_2 selectivity (S_{H_2}) in ethanol reforming; the setup is according to literature. Three catalysts using CeO_2 nanorods (1), nanacubes (2) and irregular particles (3) were prepared. Figure 2 presents the effect of the C/O ratio on the catalytic performance of Rh/ CeO_2 catalysts 1-3 (5 % mass). The C/O ratio was varied from 0.5 to 1.0. The results indicate that, for catalysts 1 and 2, S_{H_2} increased gradually on increasing C/O to reach the maximum values 124 % and 122 % at C/O = 0.7, respectively, which are larger than the maximum S_{H_2} of catalyst 3 (S_{H_2} = 116 % at C/O ratio ~ 0.6). The optimized S_{H_2} for catalyst 3 is consistent with the literature value. S_{H_2} of 1 decreased from 126 % to 100 % upon altering the C/O ratio from 0.7 to 1.0, whereas S_{H_2} of 2 decreased sharply from 122 % to 60 %. The rate of conversion of ethanol is hence affected by the morphology of nanocrystalline CeO_2. The poor catalytic performance of 3 is attributed to an even distribution of {111}, {110}, {100} and other surfaces for irregular CeO_2 nanoparticles, which have a concentration of {100} and {110} facets smaller than for CeO_2 rods and cubes. The effect of CeO_2 morphology on the catalytic performance of Rh/CeO_2 catalysts might reflect the surface energy and concentration of active sites on CeO_2 nanocrystals. These results indicate that the surface activity of (100)~(110) is greater than for (111) planes of CeO_2 crystal.

Figure 2. Hydrogen selectivity as a function of C/O ratio obtained over Rh/CeO_2 catalysts 1-3.
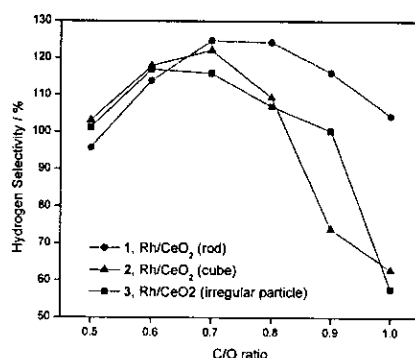
The results indicate that these catalysts as prepared show H$_2$ selectivity superior to catalysts with irregular CeO$_2$ nanoparticles. During the reforming, both the shape of CeO$_2$ particles gradually altered and the activity decreased. The {100}/{110}-dominant surface structures play a crucial role in enhancing ethanol reforming; this reaction is important for fuel-cell applications.

(三.) Ethanol to H$_2$ conversion efficiency on Rh/CeO$_2$:

Several catalysts were prepared to investigate their catalytic activity for ethanol to hydrogen conversion including A: CuO (bulk, nanoparticle) doped Al$_2$O$_3$; B: CuO doped amount on Al$_2$O$_3$; C: CuO/Al$_2$O$_3$ vs. Rh/CuO/Al$_2$O$_3$; D: CuO/Al$_2$O$_3$ vs. CuO/CeO$_2$/ Al$_2$O$_3$. We found catalysts of Rh/CuO/ Al$_2$O$_3$ and CuO/CeO$_2$/ Al$_2$O$_3$ are more reactive toward ethanol to hydrogen conversion reaction.

1. Synthesis of Metal oxide nanoparticles:

(1) Synthesis of CeO$_2$ nanorods:

A. Ce(NO$_3$)$_3$ · 6H$_2$O (1.5g) was dissolved in distilled water, and proper amounts of 10 %NaOH solution were rapidly added with stirring at about 200 rpm. After about 15 min of stirring, all of the slurry (the volume was about 35 ml) was then

46

transferred into a 50-ml autoclave.

B. heated at 100°C for 10 h. The final product was collected by filtration, washed with deionized water.

C. calcined at 350°C for 4 h.

(2) Synthesis of CuO nanoparticles:

A. $Cu(NO_3)_2$ 100ml add $NH_3 \cdot H_2O$ solution and NaOH to djust pH 9~10, and then get the precursor $Cu(OH)_2$.

B. Heat the precursor at 300°C 5hr.

(3) Synthesis of Cu_2O nanoparticles:

A. 0.25ml 0.01M $CuSO_4$ + 9ml XM CTAB（X= 0.02, 0.04, 0.06, 0.08, 0.1）+ 0.5ml 0.1M sodium ascorbate and heat to 55°C for 5min.

B. add 0.2ml 0.5M NaOH and keep Temp. for 10min.

C. remove the solution from hot-plate and wait for 30min.

D. centrifugation 6000 rms for 15min and get the product.

2. Catalyst preparation:

Metals were then coated on the supports(Al_2O_3) using an aqueous solution of metal salts ($Ce(NO_3)_3$, $Rh(NO_3)_3$, $Cu(NO_3)_2$). The solution was dripped onto the support repeatedly, allowing the water to evaporate between applications. The monolith was then heated at 400°C for 6 h in a closed furnace. A calculated amount of metal salt was used to ensure a 5 wt% metal loading based on the mass of the monolith. For the catalysts combining metal with ceria, ceria was added before the metals, using a solution of $Ce(NO_3)_3$, followed by heating for 6 h at 400°C in a closed furnace.

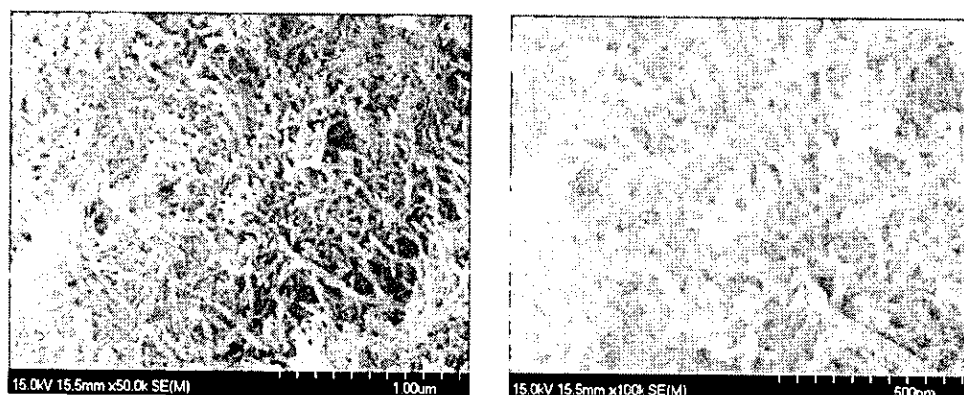# 3. Results and discussions:

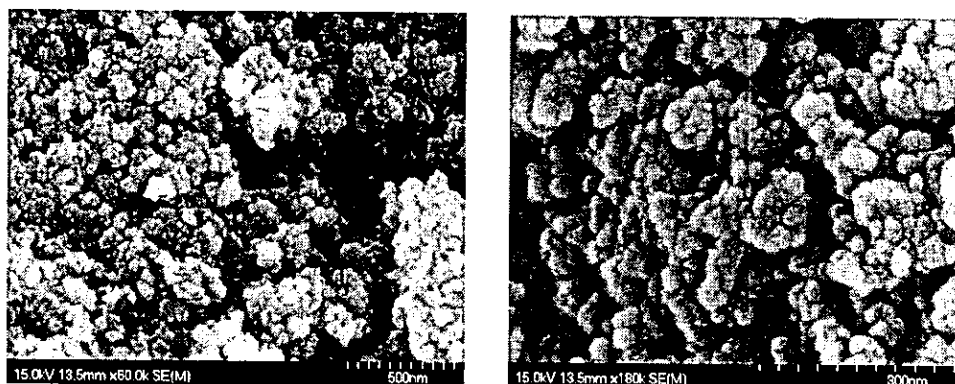## (1) Metal oxide:

Figure 3. CeO$_2$ nanorods SEM image

Figure 4. CuO nanoparticles SEM image

Table 1. Different concentration of CTAB, and morphology change of Cu$_2$O

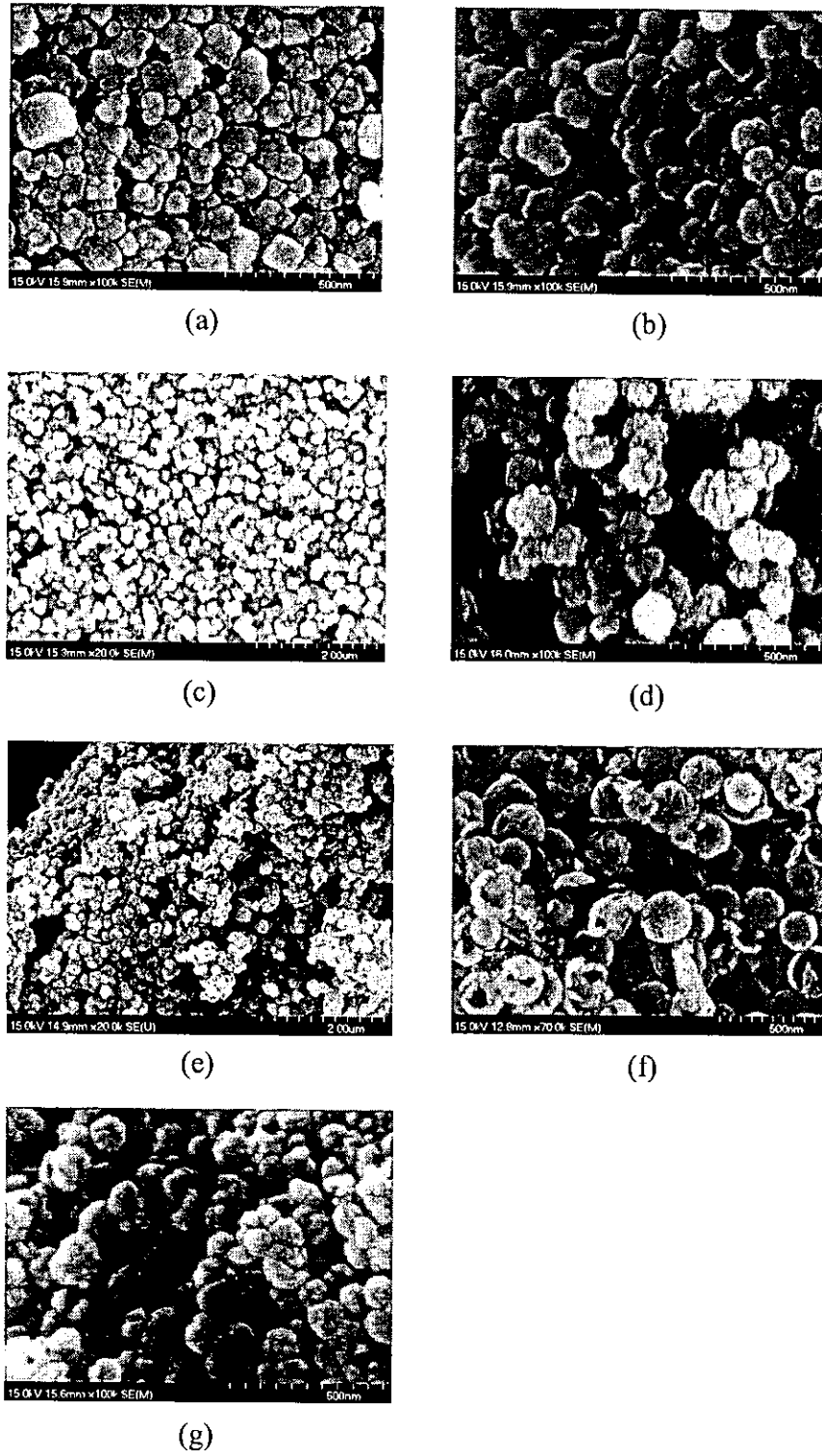| Conc. of CTAB	Morphology of Cu$_2$O
0.02 M	Aggregating particle
0.04 M	Aggregating particle
0.06 M	Cubic
0.08 M	Aggregating particle
0.10 M	Hollow sphere
0.15 M	Sphere particle
0.20 M	Hollow sphere

Fig. 5 (a) 0.02 M (b) 0.04 (c) 0.06 M (d) 0.08 M (e) 0.1 M (f) 0.15M (g) 0.2 M CTAB concentration and SEM image of Cu_2O nanoparticles.

(2) Catalysts:

Catalysts	
Standard	Schmidt's catalyst : $Rh/CeO_2/Al_2O_3$
A.	CuO (bulk, nanoparticle) doped Al_2O_3
B.	CuO doped amount on Al_2O_3
C.	CuO/Al_2O_3 vs. $Rh/CuO/Al_2O_3$
D.	CuO/Al_2O_3 vs. $CuO/CeO_2/Al_2O_3$

A. bulk CuO nanoparticles don't dope on Al_2O_3 well, and no hydrogen signal.

B. We found catalysts of $Rh/CuO/Al_2O_3$ and $CuO/CeO_2/Al_2O_3$ are more reactive toward ethanol to hydrogen conversion reaction.

4. Future plan:

(1) Determine Cu, Au, or Ag/CuO H_2 Selectivity.

(2) Add γ-Al_2O_3 and different % ZnO, test H_2 selectivity.

(3) Use Mteal oxide / TiO_2 replace Metal oxide / Al_2O_3 and compare two catalyst H_2 selectivity effect.

參、主要發現與結論

本計算團隊已穩固地建立，已經在乙醇轉氫、量子點-二氧化鈦太陽能系統及 SCC-DFTB 計算程式的研發等三大方向，因為這些大系統的計算需要龐大的計算硬體及時間，SCC-DFTB 計算程式研發後，計算的結果可與 VASP/CASTEP 固態系統的結果比較，這種比較目前仍無法做到。

因為上述大系統計算需要很大的電腦系統，核能所在這方面如果能有效供應所需的 CPU's，則對這方面的發展，將有很大的幫助。

在實驗方面，Schmidt 乙醇轉氫的實驗結果已完全證實，在未來的一年，新的催化劑 $(CuO_x / CeO_2 / Al_2O_3)$ 將被利用作一系列完整的實驗。

肆、參考文獻

1. G. A. Deluga, J. R. Salge, L. D. Schmidt, X. E. Verykios, Science, **2004**, 303, 993.

2. Jeng-Han Wang and M. C. Lin, ChemPhysChem, 2004, 5, 1615

3. Bader, R.F.W. Atoms in Molecules–A Quantum Theory, Oxford University Press, Oxford, **1990**.

4. Blyholder, G. J. Phys. Chem., **1995**, 68, 2772.

5. Hammond, G. S. J. Am. Chem. Soc., **1955**, 77, 334.

6. Liu, Z. –P.; Jenkins, S. J.; King, D. A. Phys. Rev. Lett., **2005**, 94, 196102.

7. Gorte, R. J.; Zhao S. Catal. Today, **2005**, 104, 18.

8. S. Kim, D. C. Sorescu, O. Byl, J. T. Yates, Jr. J. Phys. Chem., B **2006**, 110, 4742-4750

9. S. Kim, O. Byl, J. T. Yates, Jr. J. Phys. Chem. B, **2005**, 109, 6331-6333

10. M. Digne, P. Sautet, P. Raybaud, P. Euzen, H. Toulhoat Journal of Catalysis, **2004**, 226, 54–68

11. A. E. Nelson, K. H. Schulz Applied Surface Science, **2003**, 210 206-221.

12. Q. Ye, Q. Gao, X. R. Zhang, B. Q. Xu Catalysis Communications, **2006**, 7 589-592.

13. T. Huang, Adv. X-ray Anal., **1990**, 33, 295.

14. T. Kangas, K. Laasonen, A. Puisto, H. Pitkanen, and M. Alatalo, Surf Sci., **2005**, 584, 62.

15. Noge Cruz Hernandez and Javier Fdez. Sanz., J. Phys. Chem. B., **2002**, 106, 11495.

16. Adham Hashibon, Christian Elsasser, Manfred Ruhle., Acta Materialia., **2005**, 53, 5323.

17. J. S. Lin,W. C. Chou, S. Y. Lu, G. J. Jang, B. R. Tseng, Y. T. Li, J. Phys. Chem. B (In press).

18. M. Elstner, D. Porezag,G. Jungnickel, J. Elsner, M. Haugk, T. Frauenheim, S. Suhai, G. Seifert, Phys. Rev. B, 1998, 58, 7260

19. C. Köhler, G. Seifert, U. Gerstmann, M. Elstner, H. Overhof, T. Frauenheim, Phys. Chem. Chem. Phys., 2001, 3, 5109

20. D. Porezag, T. Frauenheim, T. Köhler, G. Seifert, R. Kaschner, Phys. Rev. B, 1995, 51, 12947-12957

21. H. Witek, K. Morokuma, and A. Stradomska, J. Chem. Phys., 2004, 121, 5171

22. H. Witek, S. Irle, G. Zheng, B. de Jong, and K. Morokuma, J. Chem. Phys., 2006, 125, in press

23. J. Desclaux, Comp. Phys. Comm., 1969, 1, 216

24. E. Malolepsza, H. Witek, and K. Morokuma, Chem. Phys. Lett., 2005, 412, 237

25. E. Malolepsza and H. Witek, in preparation